Materials Advances

ROYAL SOCIETY OF CHEMISTRY

PAPER

View Article Online
View Journal | View Issue

Open Access Article. Published on 04 March 2025. Downloaded on 1/13/2026 11:40:28 AM.
This article is licensed under a Creative Commons Attribution-NonCommercial 3.0 Unported Licence.

Check for updates

Cite this: *Mater. Adv.*, 2025, **6**, 2356

Fe-porphyrin-derived carbon nanofiber-based nanozymes: enhanced peroxidase-like activity for ultrasensitive glucose and ascorbic acid sensing†

Pradeep Singh Thakur [a] and Muniappan Sankar *[ab]

Received 28th December 2024,
Accepted 3rd March 2025

DOI: 10.1039/d4ma01289e

rsc.li/materials-advances

The development of efficient nanozymes for biomedical applications has garnered significant attention due to their exceptional stability and ease of storage, offering a compelling alternative to natural enzymes, which are often costly and functionally limited. In this study, we report the fabrication of Fe-porphyrin-derived carbon nanofibers (Fe-P/CNFs) as a nanozyme. These nanofibers exhibit a uniform one-dimensional morphology and demonstrate excellent catalytic performance in the oxidation of peroxidase substrates. Leveraging this enhanced peroxidase-like activity, we developed a highly sensitive colorimetric sensor for glucose detection, achieving a detection limit of 2.55 μM within a linear range of 0–200 μM. Additionally, Fe-P/CNFs exhibit robust performance as an ascorbic acid sensor, with a detection limit of 0.17 μM. These findings underscore the promise of Fe-P/CNFs as versatile and efficient nanozymes, making them strong candidates for practical applications in biosensing and clinical diagnostics.

Introduction

In recent years, the exploration and development of nanomaterials with enzyme-like activities, termed as nanozymes, have emerged as a promising frontier in the field of biomedicine, diagnostics, and environmental monitoring.[1–7] These nanozymes combine the advantages of both conventional enzymes and nanomaterials, offering enhanced catalytic efficiency, robust stability, and tunable properties, thereby overcoming the limitations associated with natural enzymes.[8–11] Among various nanozymes, carbon-based nanomaterials have attracted considerable attention due to their exceptional physical and chemical properties, including high surface area, excellent electrical conductivity, and biocompatibility.[12–14] Carbon nanofibers (CNFs), in particular, have garnered interest for their unique one-dimensional structure, which facilitates electron transfer and enhances catalytic activity.[15–17] Furthermore, the integration of functional molecules or metal complexes into CNFs can further enhance their catalytic performance, paving the way for the development of advanced nanozyme-based sensing platforms.[18–22]

Glucose and ascorbic acid are vital biomolecules involved in numerous physiological processes and metabolic pathways.[23,24] Accurate and sensitive detection of these analytes is crucial for monitoring health conditions, disease diagnosis, and therapeutic drug monitoring.[25,26] The primary fuel for energy consumption is glucose. Several studies have shown that glucose concentrations in body fluids such as tears, saliva, sweat and blood can act as a biomarker for metabolic state and the overall health of the body.[26,27] For example, abnormal glucose levels such as hyperglycemia or hypoglycemia can indicate underlying metabolic disturbances. It may be associated with conditions such as diabetes mellitus, metabolic syndrome, or insulin resistance.[28,29] Similarly ascorbic acid (AA) is one of the significant antioxidants, fundamental to the biosynthesis of vital bioactive compounds and commonly known as vitamin C. It acts as an essential antioxidant in humans and plays a crucial role in scavenging reactive oxygen species (ROS), such as hydroxyl radicals, superoxide radicals and singlet oxygen. Several diseases such as diabetes mellitus, cognitive impairment, coronary heart disease, and age-related cataracts have been linked to decreased levels of ascorbic acid. Thus, monitoring the levels of glucose and ascorbic acid is essential for managing diabetes mellitus and chronic metabolic disorders.

Traditionally, the detection of glucose and ascorbic acid has been accomplished with the use of absorption spectrophotometry assays and the high-performance liquid chromatography (HPLC) technique. These methods often suffer from limitations such as complex enzyme preparation, limited stability, and susceptibility to interference from other compounds.[13] Therefore, there is an increasing demand for developing alternative sensing platforms that offer improved sensitivity, selectivity, and operational simplicity. In this context, nanozyme-based sensing platforms have emerged as promising alternatives to traditional

[a] *Centre for Nanotechnology, Indian Institute of Technology Roorkee, Roorkee-247667, India. E-mail: m.sankar@cy.iitr.ac.in*

[b] *Department of Chemistry, Indian Institute of Technology Roorkee, Roorkee-247667, India*

† Electronic supplementary information (ESI) available: Materials, characterization, details on experimental procedures, and supplementary data and figures. See DOI: https://doi.org/10.1039/d4ma01289e

© 2025 The Author(s). Published by the Royal Society of Chemistry

Open Access Article. Published on 04 March 2025. Downloaded on 1/13/2026 11:40:28 AM.
This article is licensed under a Creative Commons Attribution-NonCommercial 3.0 Unported Licence.

enzymatic methods for biomolecule detection. The enhanced peroxidase-like activity of nanozymes can catalyse the oxidation of peroxidase substrates, producing colorimetric or electrochemical signals proportional to the analyte concentration. Moreover, the unique properties of nanozymes, such as high stability, reusability, and ease of functionalization, make them ideal candidates for developing ultrasensitive and selective biosensors for glucose and ascorbic acid detection.[30,31]

Porphyrins, a class of macrocyclic organic compounds, have been extensively studied for their versatile applications in catalysis, sensing, and biomedical imaging.[32–34] Their ability to bind various metal ions at the centre makes them suitable candidates for the design of metalloporphyrin-based biosensors and nanozymes.[35–37] Among various metalloporphyrins, iron (Fe)-porphyrins have been recognized for their remarkable catalytic properties, resembling those of natural peroxidases.[38,39] However, the practical applications of Fe-porphyrins are often hindered by their poor solubility, stability, and aggregation tendency in aqueous solutions.[40]

To address these challenges, porphyrin-derived carbon nanofibers (CNFs) are considered a viable and effective approach. These nanofibers are typically synthesized through a two-step process involving electrospinning of porphyrin-based precursors followed by pyrolysis. This method not only enhances the mechanical and electrical properties of the resulting CNFs but also allows for the incorporation of porphyrin's catalytic properties into the carbon structure. The one-dimensional structure of CNFs can provide a favorable environment for the immobilization of metalloporphyrins, preventing their self-aggregation and improving their accessibility to substrates. Recently, Bu and Feng synthesized micron-scale cubic structures of the CPM-99 MOF using *meso*-tetrakis(4-carboxybiphenyl)porphyrin (FeTCBPP). Upon pyrolysis, CPM-99 retains its cubic morphology, with minimal aggregation observed at the iron centers.[41] Similarly, Jiang and collaborators synthesized heat-treated nanorods of the PCN-222 MOF, derived from iron *meso*-tetrakis(4-carboxyphenyl)porphyrin (FeTCPP) and TCPP, resulting in carbonized nanorods with atomically dispersed Fe sites. In the PCN-222 MOF, TCPP effectively separates FeTCPP units, preventing agglomeration of metal centers during the pyrolysis process.[42]

Due to their porous structures, large specific surface area, abundant active sites, and ability to form heterostructures, porphyrin-derived CNFs can offer enhanced catalytic performance and stability. These properties make them highly valuable in various electrochemical catalytic processes and devices, including oxygen reduction reactions,[43–46] hydrogen production,[47,48] zinc–air batteries,[49] *etc.*[50] Apart from them, porphyrin-derived CNFs can also serve as a robust platform for various enzyme mimicking-based biosensing applications due to their unique structural and functional properties. Moreover, the interaction between metalloporphyrins and CNFs can lead to electronic modulation, thereby optimizing the redox properties and catalytic activity of the nanozymes.

This work presents the synthesis and characterization of Fe-porphyrin-derived carbon nanofiber (CNF)-based nanozymes, highlighting their application in ultrasensitive glucose and ascorbic acid sensing. Porphyrin-derived carbon nanofibers were first fabricated by incorporating iron (Fe) *meso*-tetrakis(4-hydrazidocarbonylphenyl)porphyrin (FeTHCPP) into a polyacrylonitrile (PAN) matrix using the electrospinning technique, followed by thermal treatment to convert them into CNFs. Comprehensive characterization of the Fe-porphyrin/CNF nanozymes was performed to elucidate their structural and catalytic properties. Furthermore, their catalytic performance was systematically evaluated, demonstrating their potential as innovative catalysts for advancing bioanalytical chemistry and biosensor technology.

Results and discussion

Synthesis and characterization

Electrospinning is a versatile and widely employed technique for producing nanofibers with diameters ranging from nanometres to micrometres.[51–55] This process involves the application of a high-voltage electric field to a polymer solution or melt, which is ejected from a spinneret to form a fine jet. As the jet travels towards a grounded collector, solvent evaporation or cooling leads to the solidification of the polymer, resulting in the formation of continuous fibers.[55–57]

In this study, we synthesized Fe-porphyrin-derived carbon nanofibers (Fe-P/CNFs) using a two-step method, illustrated in Scheme 1. Initially, Fe-porphyrin electrospun nanofibers (Fe-P NFs) were made by adding Fe-THCPP into the polyacrylonitrile (PAN) polymer solution and stirred continuously overnight, and the resulting solution was then injected into the jet, and electrospinning was carried out under an 18 kV voltage. The resulting Fe-porphyrin nanofibers (Fe-P NFs) were stabilized under vacuum at 100 °C to ensure thorough drying and removal of any solvent residues. Finally, the Fe-porphyrin nanofibers were transformed into Fe-porphyrin-derived carbon nanofibers (Fe-P/CNFs) by undergoing a calcination process. PAN nanofibers were also synthesized, like the Fe-P NFs but without the addition of FeTHCPP.

To elucidate the basic properties of the nanofibers such as morphology and molecular structure, SEM analysis was employed. As depicted in Fig. 1a, the electrospun PAN nanofibers (NFs) exhibit smooth surface and continuous uniform one-dimensional morphology characterized by a large length-to-diameter ratio, with diameters ranging from 90 to 130 nm.

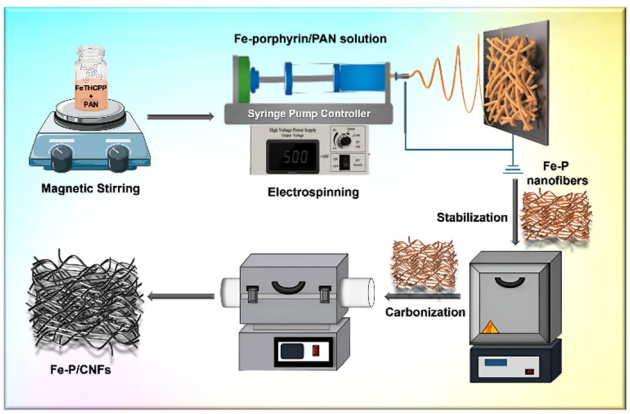

Scheme 1 Schematic representation of Fe-P/CNF formation.

Open Access Article. Published on 04 March 2025. Downloaded on 1/13/2026 11:40:28 AM.
This article is licensed under a Creative Commons Attribution-NonCommercial 3.0 Unported Licence.

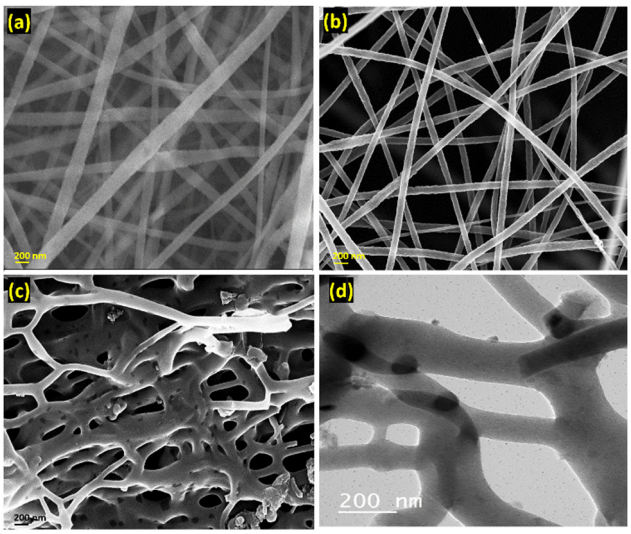

Fig. 1 Morphological characterizations of the relevant nanofibers. SEM image of (a) PAN electrospun nanofibers, (b) Fe-P electrospun nanofibers, (c) Fe-P/CNFs and (d) TEM image of Fe-P/CNFs.

Upon adding the Fe-porphyrin, the morphology of the resultant Fe-P NFs remained largely unchanged, while the sample color transitioned from white to light brown (Fig. 1b). Following the calcination process, Fe-P/CNFs show somewhat rough surface morphology, and the color of the samples shifted to black, accompanied by a slight increase in fiber diameter. The diameters of the Fe-P/CNFs ranged from 110 to 220 nm, as shown in Fig. 1c and d.

HR-TEM measurement was used to define the intricate morphology of the nanofibers. A careful examination of the HR-TEM image reveals a weakly ordered structure (Fig. 2c). Further investigation using high-angle annular dark-field scanning transmission electron microscopy (HAADF-STEM) is presented in Fig. 2a and b. These images illustrate that the resultant Fe-P/CNFs are mostly amorphous in nature.

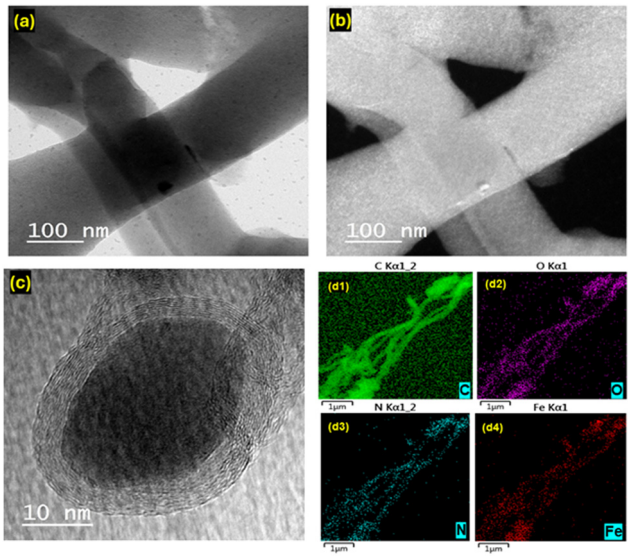

Fig. 2 HAADF-STEM image of Fe-P/CNFs: (a) bright field, (b) dark field, (c) HR-TEM image of Fe-P/CNFs, EDX element mapping of (d1) C–K, (d2) O–K, (d3) N–K and (d4) Fe–K in Fe-P/CNFs.

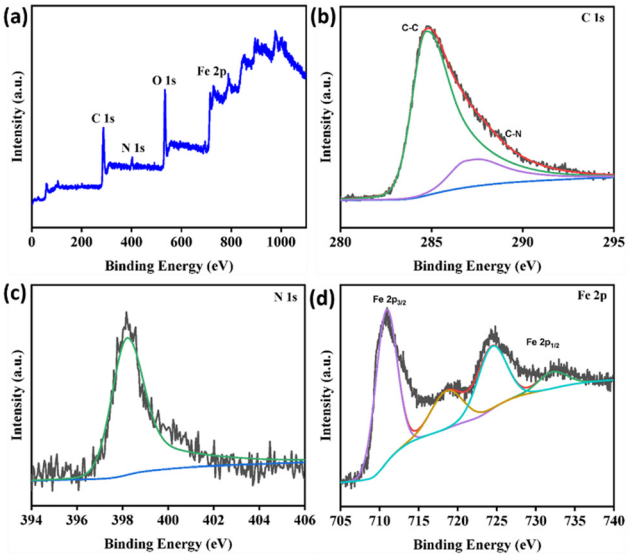

Fig. 3 (a) XPS survey spectra for Fe-P/CNFs. (b) High resolution XPS spectra for the C 1s region. (c) High resolution XPS spectra for N 1s. (d) High resolution XPS spectra for Fe 2p.

STEM energy dispersive X-ray analysis (EDX) was employed to investigate the composition of these nanofibers. Elemental mapping confirmed the presence of carbon (C), nitrogen (N), oxygen (O), and iron (Fe) in the material, as shown in Fig. 2(d1)–(d4). The STEM-EDX images demonstrate that these elements are uniformly distributed throughout the Fe-P/CNFs structure, indicating a consistent and homogeneous composition.

X-ray photoelectron spectroscopy (XPS) was employed to investigate the electronic structure of the individual elements within the material. The XPS analysis (Fig. 3) revealed characteristic peaks corresponding to the elements C, N, O, and Fe in the survey spectrum. These findings are consistent with the results obtained from EDS analysis. Furthermore, the high-resolution XPS spectra for Fe 2p reveals that Fe $2p_{3/2}$ and Fe $2p_{1/2}$ indicated at the binding energy of 710.9 eV and 724.6 eV respectively is attributed to the presence of Fe(III) in the core of the ring. Meanwhile, the two broad peaks at 732.4 eV and 718.7 eV are attributed to satellite peaks of Fe(III). In Fig. 3b, the high-resolution C 1s spectrum is deconvoluted into four peaks at 284.6, 284.9, 287.2, and 288.1 eV, corresponding to C–C, C–N, C–O, and C=O bonds, respectively. The high-resolution XPS spectrum for N 1s shows bands at 398.2 eV (Fig. 3c), attributed to porphyrinic bonds.

Peroxidase-like enzyme mimetic activity of Fe-P/CNFs

To demonstrate that Fe-P/CNFs are ideal for enzyme mimetic biosensing platforms, we assessed the peroxidase-like activity of Fe-P/CNFs and compared it to horseradish peroxidase (HRP), which is a classic example of plant peroxidases.[58] The synthesized nanozymes Fe-P/CNFs showed high peroxidase-mimicking activity, which catalyzed the decomposition of H_2O_2 to produce

 © 2025 The Author(s). Published by the Royal Society of Chemistry

Open Access Article. Published on 04 March 2025. Downloaded on 1/13/2026 11:40:28 AM.
This article is licensed under a Creative Commons Attribution-NonCommercial 3.0 Unported Licence.

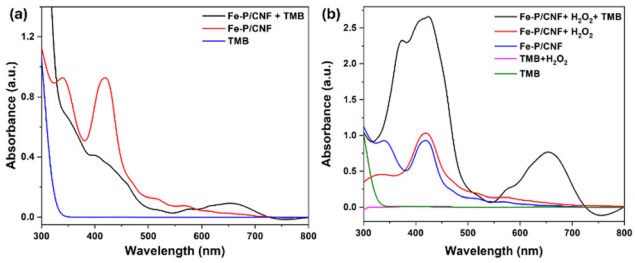

Fig. 4 UV-vis spectra of different solutions in acetate buffer (pH = 4.0) containing any two of TMB, H_2O_2, and Fe-P/CNFs: (a) oxidase-like activity and (b) peroxidase-like activity.

reactive oxygen species (ROS), which oxidises the colourless 3,3,5,5-tetramethylbenzidine (TMB) to blue oxidised TMB (ox-TMB). Based on this property, the role of Fe-P/CNFs as nano-opto-sensors was established.

Optimization of peroxidase-mimicking activity

To assess the peroxidase-mimicking activity of the synthesized nanozyme control experiments were performed using TMB and hydrogen peroxide. TMB is a chromogenic compound which on oxidation produces the blue hue in the acidic system and produces a characteristic absorption peak at 652 nm. It is worth noticing that there is no colour change and hence no prominent peak at around 650 nm in the absence of either of the Fe-P/CNF nanozyme or TMB or H_2O_2. However, when the system containing Fe-P/CNF nanozyme and TMB is exposed to sunlight for 2 min, it changes its colour to green and indicates its oxidase like activity. Furthermore, when H_2O_2 is added to the system in the usual conditions, it emphasises the peroxidase nature of the enzyme mimic. This highlights the indispensable presence of both H_2O_2 and Fe-P/CNF nanozyme for TMB oxidation (Fig. 4).

The catalytic activity, like other peroxidase-mimicking enzymes, must be dependent on physicochemical factors such as time, pH, and temperature.[59,60] The experimental conditions were optimised at different pH and temperatures to examine the effect of these factors on the catalytic activity. The results indicate that the nanozyme shows maximum activity at pH 4 and a temperature of 35–45 °C (Fig. S10, ESI†). Further temperature elevation decreased the catalytic activity.

The change in the absorbance at 652 nm with the change in time is evaluated. It is observed that the activity linearly increases up to 20 minutes (Fig. 5). We have performed control experiments to evaluate the individual catalytic contributions of Fe-porphyrin (FeTHCPP) and carbon nanofibers (CNFs). The results confirm that Fe-porphyrin alone exhibits minimal catalytic activity, while carbon nanofibers alone show negligible oxidation capability (Fig. S11, ESI†). The Fe-P/CNFs exhibit markedly enhanced catalytic performance, emphasizing the vital synergy between Fe-porphyrin and CNFs. This confirms that their integration is essential for superior activity.

Steady-state kinetic analysis of Fe-P/CNFs

The catalytic behavior of the studied nanofibers was further explored using kinetic theory and calculating the corresponding

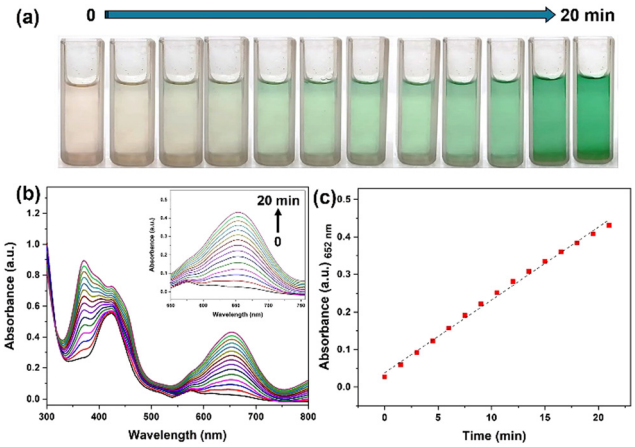

Fig. 5 (a) Time-dependent colour change of the Fe-P/CNFs-TMB-H_2O_2 system. (b) UV-vis absorption spectra in acetate buffer (pH = 4.0), and (c) corresponding plot (absorbance at 652 nm *versus* time) for studying the effect of time on the peroxidase-like activity.

steady-state kinetic parameters. By varying the concentration of one substrate and maintaining the fixed concentration for the other, the kinetics of catalytic behavior can be studied and hence, desired parameters (Michaelis constant, K_m and maximum velocity, V_{max}) can be calculated using the corresponding Lineweaver–Burk plots (Fig. 6). The constant, K_m and the maximum initial velocity were computed using the intercept and the slope of the double-reciprocal plots, respectively. K_m represents the affinity of the substrate *i.e.*, the lower the value of the constant, the stronger the binding affinity.

The K_m values of the Fe-P/CNF nanozyme calculated for TMB and H_2O_2 were 2.54 mM and 0.184 mM respectively. The K_m value obtained for the substrate H_2O_2 is drastically decreased compared to the natural HRP (3.7 mM). This indicates that a very small concentration of H_2O_2 is required to obtain the

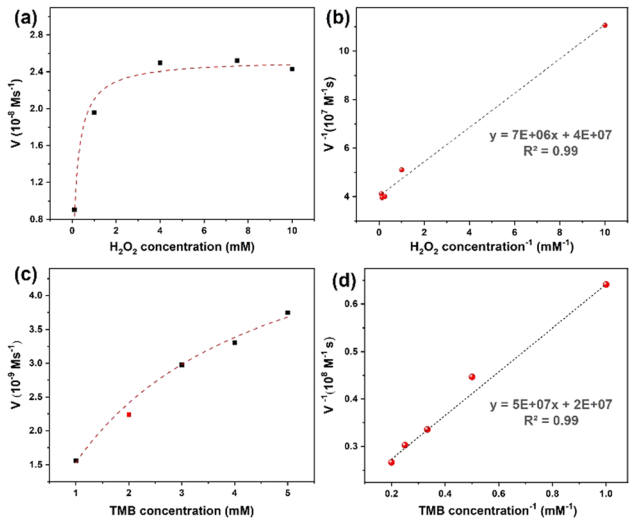

Fig. 6 Steady-state kinetic studies of the peroxidase-like experiment of the as obtained Fe-P/CNFs by using the Michaelis–Menten model by varying the concentration of (a) H_2O_2, and (c) TMB; and Lineweaver–Burk plots at different concentrations of (b) H_2O_2, and (d) TMB.

Open Access Article. Published on 04 March 2025. Downloaded on 1/13/2026 11:40:28 AM.
This article is licensed under a Creative Commons Attribution-NonCommercial 3.0 Unported Licence.

maximal peroxidase-like activity. Besides, V_{max} is the representation of the rate of reaction at the point of highest turnover. The V_{max} values were determined to be 2.5×10^{-8} M s^{-1} and 5.52×10^{-8} M s^{-1} towards peroxide and the TMB substrate, respectively. The K_m and V_{max} values were compared to the previous literature and are tabulated in Table S2 (ESI†).

Colorimetric estimation of glucose and selectivity

Colorimetric glucose biosensors primarily rely on natural enzymes to detect glucose and chromophores to identify the resulting enzymatic reaction products.[61] But the extensive application of many natural enzymes is limited by the inherent defects. The use of nanozymes for colorimetric detection has gained popularity recently because of many advantages such as high sensitivity, stability under rigid reaction conditions, adaptability with inexpensive materials and tunable catalytic activity.[62,63]

Thus, peroxidase-like activity of the studied nanozyme can be further extended to explore the glucose detecting ability of these nanofibers. At the optimum pH and aerobic conditions, glucose can be oxidised to gluconic acid in the presence of glucose oxidase (GO_x).[64] In the process, one equivalent of H_2O_2 is liberated, which can be further detected using the catalyst and TMB to produce oxidised TMB indicated by blue colour. With the gradual increase in glucose concentration from 0 to 600 μM, the colour intensity of the sample increases. The spectral plot of variation in absorbance with respect to the glucose concentration is shown in Fig. 7a. The absorbance at 652 nm varies in a linear progression up to 200 μM concentration of glucose. After 400 μM, it becomes apparently constant.

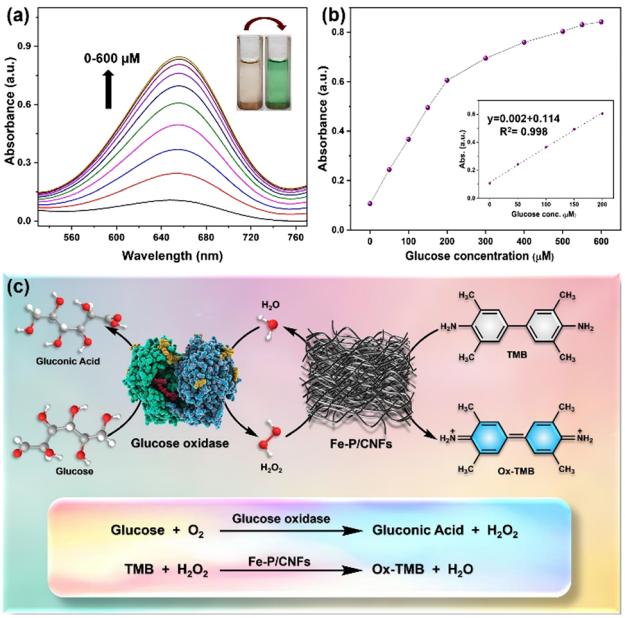

Fig. 7 Glucose detection assay of the Fe-P/CNFs. (a) UV spectra of solutions containing different amounts of glucose from 0 to 600 μM (the inset shows the colour change of the solutions with increased glucose concentration), (b) the corresponding calibration curve (the inset shows the linear fit range from 0 to 200 μM), and (c) representation scheme depicting the mechanism of glucose detection.

For glucose detection, the limit of detection (LOD) was observed to be 2.55 μM. The enhanced sensitivity of the glucose detection system can be attributed to the presence of multiple active sites and the ultrathin fibrous structure of the peroxidase mimic nanozyme developed in this study. Given that glucose concentrations in the blood of diabetic individuals typically range from 9 to 40 mM, while in healthy individuals it is around 3 to 8 mM, the colorimetric sensor designed here is sufficiently sensitive to accurately detect glucose levels in serum.

Table S3 (ESI†) provides a comprehensive comparison, showcasing the limits of detection (LOD) achieved with various porphyrin nanocomposites, including nanoparticles, nanorods, and nanosheets, alongside other examples. Notably, to the best of our knowledge, no prior studies have reported the use of porphyrin-derived carbon nanofibers for glucose detection. Compared to existing studies, the glucose sensing performance demonstrated in this work exhibits comparable sensitivity.

When comparing the glucose sensing performance in this study with previous reports (Table S3, ESI†), it becomes clear that the sensitivity observed here is on par with other porphyrin-based biosensors. The results demonstrate that Fe-porphyrin-derived CNFs hold promise as a sensitive and efficient material for glucose sensing, with performance comparable to or even exceeding that of other more widely studied porphyrin-based nanocomposites.

Notably, Fe-/CNFs nanozymes exhibit remarkable selectivity for glucose over its analogues, including fructose, maltose, sucrose, and lactose. Given that GOx possesses an inherently high specificity for glucose, only glucose generated a meaningful signal (Fig. 8a). Even when the concentrations of glucose analogues were increased to ten times that of glucose, no detectable response was observed (Fig. 8b). The results show that this novel biosensor technology opens the door for future studies to explore its applications in clinical diagnostics, particularly for real-time monitoring of glucose levels.

Ascorbic acid detection assay and selectivity

Traditionally, the detection of ascorbic acid has been accomplished with the use of absorption spectrophotometry assays and the HPLC technique. However, nanozyme-based colorimetry offers a more practical and sensitive method for detection.[65] Very few reports are available in the literature for the optical

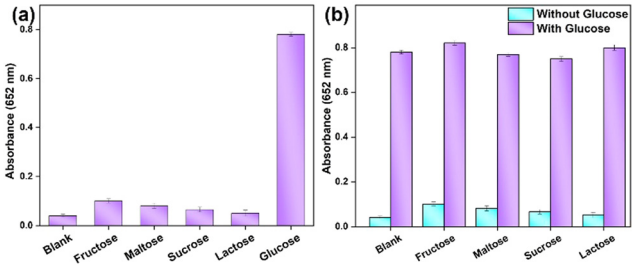

Fig. 8 (a) Selectivity analysis of the Fe-P/CNFs nanozyme for glucose detection against other potential interfering sugars. (b) Comparison of A_{652} nm values for 10 times higher concentrations of other potential interfering sugars with and without glucose.

 © 2025 The Author(s). Published by the Royal Society of Chemistry

Open Access Article. Published on 04 March 2025. Downloaded on 1/13/2026 11:40:28 AM.
This article is licensed under a Creative Commons Attribution-NonCommercial 3.0 Unported Licence.

detection of ascorbic acid which are based on porphyrins.[66] In the presented study, building on its excellent peroxidase-mimicking performance, the Fe-P/CNFs nanozyme was employed for the colorimetric detection of ascorbic acid (AA). This detection is enabled by the chromogenic reaction of the TMB substrate, facilitated by the peroxidase-like activity of the Fe-P/CNFs. In the presence of the Fe-P/CNFs and H_2O_2, TMB is oxidized to oxTMB, producing a distinct blue color (Fig. 9c). Upon the introduction of AA, the analyte reduces oxTMB back to TMB, leading to color fading and the formation of dehydroascorbic acid, as depicted in Fig. 9c. Since the degree of color change directly correlates with the AA concentration, its quantification can be achieved by monitoring the absorbance variation at 652 nm.

To evaluate it, the UV-vis spectrum of the prepared nanocatalytic system is calibrated with different ascorbic acid concentrations (0–90 μM). As shown in Fig. 9a, the progressive reduction in the absorption peak at 652 nm is evident and synchronized with the disappearance of color. In the calibration curve, a highly linear response of the relationship between the absorbance changes at 652 nm and the AA concentration is recorded. The LOD for AA is calculated as 0.17 μM ($3\sigma/S$), which surpasses most of the previously reported nanozyme-based sensing platforms (Table S4, ESI†).

To further explore its applicability, we evaluated the selectivity of Fe-P/CNF nanozymes for ascorbic acid (AA) detection in the presence of various potential interfering biomolecules, such as glutathione (GSH), dopamine, lactic acid, and folic acid (Fig. 10). Notably, even at 10-fold higher concentrations than AA, these interfering biomolecules induced no significant absorbance changes, demonstrating the Fe-P/CNF's exceptional selectivity for AA detection. Furthermore, no noticeable interference was observed. These results confirm that our colorimetric assay exhibits outstanding anti-interference properties, meeting the practical requirements for highly selective AA detection.

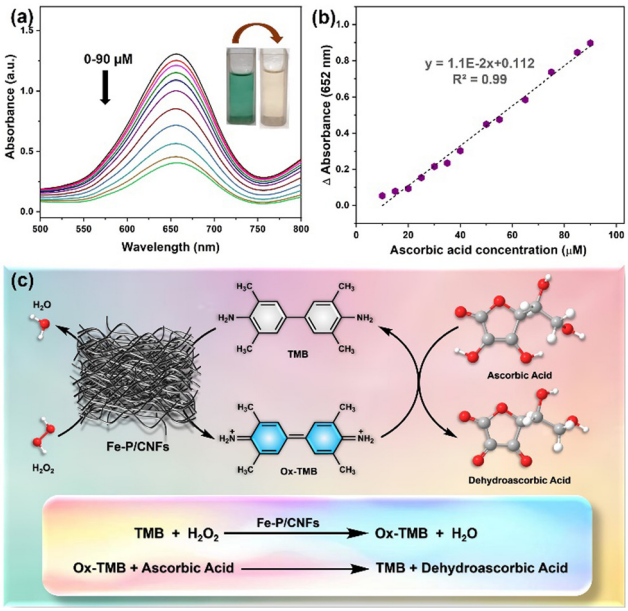

Fig. 9 (a) Absorption spectra of ox-TMB in different AA concentrations from 0–90 μM (the inset shows the color change of the solutions with increased ascorbic acid concentration), (b) corresponding linear calibration plots for AA detection, and (c) depiction scheme for ascorbic acid detection assay.

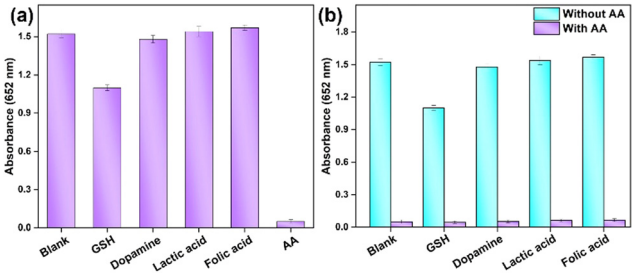

Fig. 10 (a) Selectivity analysis of the Fe-P/CNFs nanozyme for AA detection against other potential interfering biomolecules. (b) Comparison of A_{652} nm values for 10 times higher concentrations of other potential interfering biomolecules with and without AA.

Experimental

Chemicals and materials

Methyl-4-formyl benzoate and pyrrole were purchased from SRL and TCI Chemicals, India, respectively. *N,N*-Dimethylformamide (DMF), anhydrous glucose, polyacrylonitrile (PAN, MW = 80 000 g mol^{-1}), 3,3,5,5-tetramethylbenzidine (TMB), and glucose oxidase (GOx) were obtained from SRL, HiMedia, and Sigma-Aldrich and used as received. Ferric chloride (hexahydrated) was obtained from Thomas Baker. Acetic acid (CH_3COOH) and sodium acetate (CH_3COONa) were obtained from Sigma-Aldrich and utilized for the preparation of acetate buffer. All solvents were analytical grade and distilled before use. Ultrapure Milli-Q water (18.25 MΩ cm) was used throughout the experiments.

Preparation of Fe-porphyrin/PAN electrospun nanofibers (Fe-P NFs)

At first, 400 mg of PAN powder was dissolved in 5 mL of DMF, stirring at room temperature, to achieve a homogeneous and transparent solution. Then, 20 mg of Fe-THCPP was added into the above PAN solution with magnetic stirring overnight to obtain a viscous solution. The viscous solution as an electrospun precursor was filled into a 5 mL plastic syringe with a 0.6 mm diameter blunt-ended needle. The electrospun NFs containing Fe-porphyrin were prepared by using commercial electrospinning equipment. The electrospinning conditions were optimized to give non-beaded almost uniform nanofibers. Finally, the synthesis was performed under a voltage of 10–15 kV with a flow rate of 1 ml per hour and the ambient temperature and air humidity of 25–30 °C and 50–60%, respectively. The syringe and the collector were around 20 cm apart. Similarly, bare PAN-based NFs were prepared under the optimised conditions.

Open Access Article. Published on 04 March 2025. Downloaded on 1/13/2026 11:40:28 AM.
This article is licensed under a Creative Commons Attribution-NonCommercial 3.0 Unported Licence.

Preparation of Fe-porphyrin-derived carbon nanofibers (Fe-P/CNFs)

The Fe-P nanofibers obtained in the previous step were further calcinated to get the target Fe-P/CNFs. In a typical procedure, the Fe-P nanofibers were kept in a tube furnace and heated to 700–800 °C for 2 h with a heating rate of 2 °C min^{-1} in an inert atmosphere. Eventually, a black amorphous material of Fe-P/CNFs was obtained.

Optimization of the peroxidase-mimicking activity

To study the peroxidase-like activity of the Fe-P/CNFs, a control experiment is carried out using TMB and H_2O_2. For a typical experiment, 2.7 mL of acetate buffer (pH = 4.0), 100 μL TMB (5 mM), 100 μL of H_2O_2 (10 mM), and 100 μL of Fe-P/CNFs-based nanozyme (3 mg mL^{-1} in DMSO) were mixed. The solution was incubated for 10 min, and absorbance spectra were recorded. The variation of the absorbance at 652 nm was observed with increasing time, and the graph was plotted. Similarly, the effect of pH and temperature were also considered and recorded, keeping all the remaining factors constant.

Steady-state kinetic assay of Fe-P/CNFs

To analyse the kinetic behaviour of the carbon nanofibers, the steady-state kinetics were evaluated in acetate buffer (pH = 4.0), which included 100 μL of 3 mg mL^{-1} Fe-P/CNFs and various concentrations of TMB (1–5 mM) or H_2O_2 (1–100 mM) as the substrate. The Lineweaver–Burk plots were obtained according to the Michaelis–Menten plots based on the equation,

$$\frac{1}{V} = \frac{K_m}{V_m}\frac{1}{[S]} + \frac{1}{V_m}$$

where V represents the initial enzyme reaction rate at [S], [S] is the substrate concentration, V_m represents the maximum velocity, and K_m denotes the Michaelis constant. The initial velocity at different concentrations can be calculated using the Beer Lambert law, taking the molar extinction coefficient value for TMB as 39 000 M^{-1} cm^{-1}.

Colorimetric detection of glucose

For colorimetric glucose detection, 100 μL of glucose at varied concentrations were mixed with 100 μL of glucose oxidase (1 mg mL^{-1}) and incubated at room temperature for 30 minutes. Subsequently, the mixture was added to 2.1 mL of acetate buffer (pH= 4.0), 100 μL of Fe-P/CNFs (3 mg mL^{-1} in DMSO), and 100 μL of TMB (5 mM) solution. The corresponding absorption spectra of the system were recorded. The limit of detection (LOD) was determined using $3\sigma/S$ ratio, in which the σ denotes standard deviation of the blank solution and S is the slope of the calibration curve obtained for glucose titration.

Ascorbic acid detection assay

The detection of ascorbic acid was monitored by the disappearance of the blue oxidised-TMB (ox-TMB) with the consequent addition of ascorbic acid (AA). For the AA detection assay, 100 μL of Fe-P/CNFs solution was taken in 2.1 ml of acetate buffer solution and 100 μL of 5 mM TMB was added to it. It was followed by additional discharge of 100 μL of 10 mM H_2O_2 solution. After incubating the mixture for 20 min, various concentrations of AA were added successively. This is accompanied by obvious gradual fading of color from deep green to colourless, which is monitored by absorption spectral features. The limit of detection (LOD) was calculated as in the case of glucose detection.

Conclusion

To summarize, Fe-porphyrin-derived nanozyme with high peroxidase-like catalytic activity was successfully fabricated using a nanofiber synthetic strategy, based on which a highly sensitive colorimetric sensor for ascorbic acid and glucose was developed. The Fe-P/CNFs were thoroughly characterized, and their enzymatic performance was evaluated. The kinetic parameters revealed a high affinity for H_2O_2 with K_m of 0.184 mM. Compared with the natural enzyme HRP, this nanozyme shows better results in terms of hydrogen peroxide binding. Utilizing our catalyst in combination with glucose oxidase (GOx), we developed a highly sensitive and selective one-pot colorimetric assay for glucose detection with a low detection limit of 2.55 μM. Furthermore, detection of ascorbic acid showed a very low detection limit of 0.17 μM. To the best of our knowledge, there are no existing reports on the use of porphyrin-derived carbon nanofibers for the detection of glucose and ascorbic acid. This study aims to bridge that gap by providing valuable insights into the potential of exploring porphyrin nanofibers as a nanozyme for mimicking enzyme activity, encouraging further exploration of their catalytic abilities in biosensing applications.

Author contributions

P. S. T.: conceptualization, data curation, investigation, methodology, formal analysis, validation, visualization, and writing – original draft. M. S.: conceptualization, formal analysis, validation, supervision, project administration, writing – review & editing, resources, and funding acquisition.

Data availability

The data supporting this article have been included as part of the ESI.†

Conflicts of interest

There are no conflicts to declare.

Acknowledgements

PST gratefully acknowledges the Ministry of Education (MoE), Govt. of India, for providing a doctoral fellowship. MS sincerely thanks Science and Engineering Research Board (SERB/CRG/

 © 2025 The Author(s). Published by the Royal Society of Chemistry

Open Access Article. Published on 04 March 2025. Downloaded on 1/13/2026 11:40:28 AM. This article is licensed under a Creative Commons Attribution-NonCommercial 3.0 Unported Licence.

2020/005958), New Delhi, for the financial support. Sincere thanks go to Institute Instrumentation Centre, Department of Chemistry and Department of Metallurgical and Materials Engineering, Indian Institute of Technology Roorkee, for the various analytical facilities provided.

Notes and references

1 R. Zhang, X. Yan and K. Fan, *Acc. Mater. Res.*, 2021, **2**, 534–547.
2 D. Jiang, D. Ni, Z. T. Rosenkrans, P. Huang, X. Yan and W. Cai, *Chem. Soc. Rev.*, 2019, **48**, 3683–3704.
3 M. Zandieh and J. Liu, *ACS Nano*, 2021, **15**, 15645–15655.
4 A. Robert and B. Meunier, *ACS Nano*, 2022, **16**, 6956–6959.
5 X. Mou, Q. Wu, Z. Zhang, Y. Liu, J. Zhang, C. Zhang, X. Chen, K. Fan and H. Liu, *Small Methods*, 2022, **6**, 2200997.
6 M. Liu, H. Yu, T. Zhao and X. Li, *Dalt. Trans.*, 2023, **52**, 15203–15215.
7 X. Liu, Y. Gao, R. Chandrawati and L. Hosta-Rigau, *Nanoscale*, 2019, **11**, 21046–21060.
8 H. Wei and E. Wang, *Chem. Soc. Rev.*, 2013, **42**, 6060.
9 Y. Huang, J. Ren and X. Qu, *Chem. Rev.*, 2019, **119**, 4357–4412.
10 M. Liang and X. Yan, *Acc. Chem. Res.*, 2019, **52**, 2190–2200.
11 H. Fan, R. Zhang, K. Fan, L. Gao and X. Yan, *ACS Nano*, 2024, **18**, 2533–2540.
12 L. Zhang, H. Wang and X. Qu, *Adv. Mater.*, 2024, **36**, e2211147.
13 H. Ding, B. Hu, B. Zhang, H. Zhang, X. Yan, G. Nie and M. Liang, *Nano Res.*, 2021, **14**, 570–583.
14 S. V. Somerville, Q. Li, J. Wordsworth, S. Jamali, M. R. Eskandarian, R. D. Tilley and J. J. Gooding, *Adv. Mater.*, 2024, **36**, e2211288.
15 T. Wang, Z. Chen, W. Gong, F. Xu, X. Song, X. He and M. Fan, *ACS Omega*, 2023, **8**, 22316–22330.
16 Y. Zhang, Y. Jin, H. Cui, X. Yan and K. Fan, *RSC Adv.*, 2019, **10**, 10–20.
17 X. Zhang, Y. Duan, W. Dong, S. Wu, G. Xing and Q. Duan, *J. Environ. Chem. Eng.*, 2024, **12**, 113238.
18 Kenry and C. T. Lim, *Prog. Polym. Sci.*, 2017, **70**, 1–17.
19 S. Chen, Y. Wang, M. Zhong, D. Yu, C. Wang and X. Lu, *ACS Biomater. Sci. Eng.*, 2019, **5**, 1238–1246.
20 P. B. Niu, Y. Q. Wang, R. Hu and T. Yang, *ACS Appl. Nano Mater.*, 2024, **7**, 5996–6004.
21 Y. Sun, B. Xu, X. Pan, H. Wang, Q. Wu, S. Li, B. Jiang and H. Liu, *Coord. Chem. Rev.*, 2023, **475**, 214896.
22 S. Chen, Y. Wang, M. Zhong, D. Yu, C. Wang and X. Lu, *ACS Biomater. Sci. Eng.*, 2019, **5**, 1238–1246.
23 S. Khumngern and I. Jeerapan, *Commun. Mater.*, 2024, **5**, 135.
24 X. Wang, Z. Xia, E. K. Fodjo, W. Deng and D. Li, *J. Mater. Chem. B*, 2022, **10**, 3023–3031.
25 Q. Wang, H. Wei, Z. Zhang, E. Wang and S. Dong, *TrAC, Trends Anal. Chem.*, 2018, **105**, 218–224.
26 Y. J. Hong, H. Lee, J. Kim, M. Lee, H. J. Choi, T. Hyeon and D.-H. Kim, *Adv. Funct. Mater.*, 2018, **28**, 1805754.
27 F. Gao, C. Liu, L. Zhang, T. Liu, Z. Wang, Z. Song, H. Cai, Z. Fang, J. Chen, J. Wang, M. Han, J. Wang, K. Lin, R. Wang, M. Li, Q. Mei, X. Ma, S. Liang, G. Gou and N. Xue, *Microsyst. Nanoeng.*, 2023, **9**, 1.
28 C. Xiong, Q. Li, J. Yang, L. Cheng, M. Adeli, X. Luo, X. Xu, C. He and C. Cheng, *Chem. Eng. J.*, 2024, **490**, 151881.
29 M. S. Beeri and B. B. Bendlin, *Lancet Diabetes Endocrinol.*, 2020, **8**, 736–738.
30 A. Liu, W. Song, C. Zhang and H. Shang, *ACS Appl. Nano Mater.*, 2024, **7**, 13400–13406.
31 C. Tao, Y. Jiang, S. Chu, Y. Miao, J. Zhang, Y. Lu and L. Niu, *Anal. Chem.*, 2024, **96**, 3107–3115.
32 X. Zeng, T. Wang, Z. Wang, M. Tebyetekerwa, Y. Liu, Z. Liu, G. Wang, A. A. Wibowo, G. Pierens, Q. Gu and X. Zhang, *ACS Catal.*, 2024, **14**, 9955–9968.
33 R. Paolesse, S. Nardis, D. Monti, M. Stefanelli and C. Di Natale, *Chem. Rev.*, 2017, **117**, 2517–2583.
34 H. Keum, D. Yoo and S. Jon, *Adv. Drug Delivery Rev.*, 2022, **182**, 114134.
35 P. S. Thakur, L. Gautam, S. P. Vyas and M. Sankar, *Inorganic Nanosystems*, Elsevier, 2023, pp. 489–507.
36 E. Cheng, B. Li and Q. Zou, *Adv. Ther.*, 2024, **7**, 2300329.
37 P. S. Thakur and M. Sankar, *Mater. Lett.*, 2022, **311**, 131540.
38 Y. Xie, M. Xu, L. Wang, H. Liang, L. Wang and Y. Song, *Mater. Sci. Eng., C*, 2020, **112**, 110864.
39 Y. Zheng, J. Zheng, M. Du, Y. Yang, X. Li, H. Chen and Y. Gao, *J. Mater. Chem. B*, 2023, **11**, 4958–4971.
40 M. Aghayan, A. Mahmoudi, S. Sohrabi, S. Dehghanpour, K. Nazari and N. Mohammadian-Tabrizi, *Anal. Methods*, 2019, **11**, 3175–3187.
41 Q. Lin, X. Bu, A. Kong, C. Mao, X. Zhao, F. Bu and P. Feng, *J. Am. Chem. Soc.*, 2015, **137**, 2235–2238.
42 L. Jiao, G. Wan, R. Zhang, H. Zhou, S.-H. Yu and H.-L. Jiang, *Angew. Chem., Int. Ed.*, 2018, **57**, 8525–8529.
43 M. Li, Z. Xiao, L. Fan, F. Wang, X. Du, Z. Kang, W. Fan, Z. Guo and D. Sun, *Inorg. Chem. Front.*, 2019, **6**, 2296–2303.
44 H. Han, Y. Zhang, Y. Cong, J. Qin, Z. Zhai, X. Wang, R. Gao, G. Zhang, X. Guo and Y. Song, *Catal. Sci. Technol.*, 2020, **10**, 7160–7164.
45 C. Ling, W.-Y. Xie, S.-F. He, G.-C. Liang, X.-Y. Xiao, C.-L. Yang and H.-Y. Liu, *J. Alloys Compd.*, 2024, **987**, 174172.
46 S. Brüller, H.-W. Liang, U. I. Kramm, J. W. Krumpfer, X. Feng and K. Müllen, *J. Mater. Chem. A*, 2015, **3**, 23799–23808.
47 A. Wang, X. Yang, F. Zhang, Q. Peng, X. Zhai and W. Zhu, *Dalt. Trans.*, 2024, **53**, 14725–14734.
48 X. Fan, F. Kong, A. Kong, A. Chen, Z. Zhou and Y. Shan, *ACS Appl. Mater. Interfaces*, 2017, **9**, 32840–32850.
49 M. Y. Yu, Y. F. Yao, K. Fang, L. S. Chen, L. P. Si and H. Y. Liu, *ACS Appl. Mater. Interfaces*, 2024, **16**, 16132–16144.
50 J. Xu, B. Li, Z. Ma, X. Zhang, C. Zhu, F. Yan, P. Yang and Y. Chen, *Nano-Micro Lett.*, 2024, **16**, 1–18.
51 M. Yang, T. Zhao, W. Xia, K. Wei, R. Li, W. Jiang, C. Zhou, H. Ben, J. Zhang, S. Ramakrishna and Y. Z. Long, *Int. J. Biol. Macromol.*, 2024, **257**, 128698.
52 J. Xue, T. Wu, Y. Dai and Y. Xia, *Chem. Rev.*, 2019, **119**, 5298–5415.

Open Access Article. Published on 04 March 2025. Downloaded on 1/13/2026 11:40:28 AM.
This article is licensed under a Creative Commons Attribution-NonCommercial 3.0 Unported Licence.

53 D. Li and Y. Xia, *Nano Lett.*, 2003, **3**, 555–560.
54 J. Xue, J. Xie, W. Liu and Y. Xia, *Acc. Chem. Res.*, 2017, **50**, 1976–1987.
55 A. Luraghi, F. Peri and L. Moroni, *J. Control. Release*, 2021, **334**, 463–484.
56 L. Shang, Y. Yu, Y. Liu, Z. Chen, T. Kong and Y. Zhao, *ACS Nano*, 2019, **13**, 2749–2772.
57 P. S. Thakur and M. Sankar, *Advanced and Modern Approaches for Drug Delivery*, Elsevier, 2023, pp. 493–514.
58 L. Gao, J. Zhuang, L. Nie, J. Zhang, Y. Zhang, N. Gu, T. Wang, J. Feng, D. Yang, S. Perrett and X. Yan, *Nat. Nanotechnol.*, 2007, **2**, 577–583.
59 Z. Chen, J. J. Yin, Y. T. Zhou, Y. Zhang, L. Song, M. Song, S. Hu and N. Gu, *ACS Nano*, 2012, **6**, 4001–4012.
60 C. Lu, X. Liu, Y. Li, F. Yu, L. Tang, Y. Hu and Y. Ying, *ACS Appl. Mater. Interfaces*, 2015, **7**, 15395–15402.
61 H.-J. Jeon, H. S. Kim, E. Chung and D. Y. Lee, *Theranostics*, 2022, **12**, 6308–6338.
62 H. Chen, Q. Shi, G. Deng, X. Chen, Y. Yang, W. Lan, Y. Hu, L. Zhang, L. Xu, C. Li, C. Zhou, Y. She and H. Fu, *Sens. Actuators, B*, 2021, **343**, 130104.
63 W. Zhao, G. Zhang, Y. Du, S. Chen, Y. Fu, F. Xu, X. Xiao, W. Jiang and Q. Ji, *J. Mater. Chem. B*, 2021, **9**, 4726–4734.
64 J. F. Kornecki, D. Carballares, P. W. Tardioli, R. C. Rodrigues, Á. Berenguer-Murcia, A. R. Alcántara and R. Fernandez-Lafuente, *Catal. Sci. Technol.*, 2020, **10**, 5740–5771.
65 Q. Chen, R. Lin, W. Wang, Y. Zuo, Y. Zhuo, Y. Yu, S. Chen and H. Gu, *Anal. Chem.*, 2024, **96**, 6683–6691.
66 Y. He, N. Li, J. Lian, Z. Yang, Z. Liu, Q. Liu, X. Zhang and X. Zhang, *Colloids Surf., A*, 2020, **598**, 124855.

 © 2025 The Author(s). Published by the Royal Society of Chemistry